Continuously Variable Stiffness Mechanism Using Nonuniform Patterns on Coaxial Tubes for Continuum Microsurgical Robot

Jongwoo Kim , *Student Member, IEEE*, Woo-Young Choi, *Student Member, IEEE*,
Sungchul Kang , *Member, IEEE*, Chunwoo Kim , *Member, IEEE*, and Kyu-Jin Cho , *Member, IEEE*

Abstract—Variable stiffness enables the safe and effective operation of the minimally invasive surgical instruments. In this article, we propose a continuously variable stiffness mechanism of the scalable tubular structure. The mechanism consists of multiple coaxial nitinol tubes, and each tube has an anisotropic distribution of flexural stiffness created by nonuniform through-hole patterning. The stiffness of the mechanism is varied by relative rotation and translation among the tubes, resulting in flexural stiffness difference up to 7.2 times in the direction of load. Its flexural stiffnesses along principal axes are independently controlled by the suggested counterrotation algorithm. The stiffness change is validated through analytical modeling, FEM simulation, and the experiments. Thanks to its physically embodied intelligence, the mechanism has a simple scalable structure and the response time is immediate. We applied this mechanism to control the stiffness of the steerable needle. Varying the stiffness grants the additional degree of freedom to control the needle's trajectory, which can expand the workspace of the steerable needle.

Index Terms—Mechanism design, medical robots and system, steerable catheters/needles, surgical robotics, variable stiffness mechanism.

I. INTRODUCTION

MINIMALLY invasive surgery (MIS) is becoming more popular as it has several advantages compared to traditional open surgery, such as smaller incision and faster recovery time. In MIS, continuum robots are widely used, thanks to their scalability and compactness. However, the smaller the space, the more difficult it is to control the motion of the continuum robots due to the smaller moment arm and the lack of adequate microactuators. Variable stiffness can be utilized to provide motion control for the continuum robots under interactions with nearby tissues in anatomically confined space. Under the same load, the deflection of the same-length beam increases as flexural stiffness decreases. Without activating any actuators or additional load, the motion of the beam is changed. In confined space where an additional actuator is not feasible, the variable stiffness can be an efficient solution for controlling small and delicate surgical instruments. Additionally, low stiffness is preferred for safety inside the human body and high stiffness is required to avoid buckling or in medical environments. Thus, this motivates the development of a variable stiffness mechanism which can adjust its stiffness to meet the needs imposed by varying conditions for the manipulation of meso/microscale surgical instruments. However, the stiffness control in continuum robots has been very challenging so far.

Many different variable stiffness mechanisms have been studied: some mechanisms employed shape memory materials [1], [2], fluidic flexible matrix composites [3], the combination of electrostatic forces and pneumatic forces [4], anisotropic pneumatic forces [5], tendon-drive mechanisms [6], [7], variable neutral-line mechanisms [8], layer jamming mechanisms [9], granular jamming mechanisms [10]–[13], low melting point alloys [14]–[16], modulations of polymer [17], [18], and lever mechanisms [19]. However, the current variable stiffness mechanisms have a complex structure which is very difficult to scale down to satisfy the spatial constraint of minimally invasive surgery. Also, some mechanisms use heat or high-voltage stimulus to induce stiffness change which can lead to a potential safety issue for medical usage. Additionally, shape memory polymers (SMP), conductive elastomers, and low melting point alloy have relatively long response times due to heating and cooling time; for example, the response time takes more than 17 seconds to transform from rigid state to flexible state [14]. Moreover, the current mechanisms have binary or discrete stiffness states due to difficulties of precisely controlling heat or electric stimulus, jamming effect, and pneumatic or fluidic pressure.

To overcome these limitations, we propose a variable stiffness mechanism using a coaxial set of tubes with anisotropic flexural stiffness. The mechanism consists of two or more coaxial tubes with nonuniform through-hole patterns (material removal). The nonuniform patterning on each tube creates anisotropy in flexural stiffness (EI). The stiffness of the mechanism with respect to a certain direction of load is changed by relative translation and rotation between the coaxial tubes. The proposed mechanism is distinguished from other variable stiffness mechanisms in terms of continuous variable stiffness, scalability, and response time.

First, the mechanism has continuous states of variable stiffness, instead of discrete states. Mechanisms based on electric, heat, or jamming stimulus mostly have discrete states of stiffness as it is difficult to precisely control their output from their input, or the input itself has binary or discrete states. However, the proposed mechanism precisely determines the anisotropic distribution of the flexural stiffness by relative rotation and translation of the tubes. The flexural stiffness is well defined by relative rotational angle and longitudinal position in a continuous function form.

Second, the mechanism is scalable enough to be suitable for the dimension of minimally invasive surgery. The mechanism for changing the flexural stiffness is embedded in its structure and does not require bulky pneumatic lines or electrical wirings. As a result, in this study, it was possible to scale down the mechanism to 1.8 mm diameter, sufficiently small enough to be applied to minimally invasive surgery.

Third, the response time is much shorter than other mechanisms that rely on the phase change of the material. The stiffness of the mechanism can be changed by translational and rotational movement of the tubes in a few microseconds.

The rest of this article is organized as follows. In Section II, we present the design and modeling of the mechanism. We investigated the nonuniform patterning method as a solution to the variable stiffness mechanism without bulky actuators or accessories. The flexural stiffness of the mechanism was modeled as a continuous function of the rotational configuration of the inner and the outer tubes. Section III describes the FEM simulation on the flexural stiffness of the mechanism. To verify the variation of the flexural stiffness, the simulation results are compared with the prediction from the analytical model and the experimental result from the three-point bending test. Section IV describes the laser machining setup and procedures that we used to pattern the nitinol tubes and showed how the mechanism was assembled. Additionally, we set up the control system to control the relative rotational and translational movement of the tubes. A load test was performed to demonstrate the continuous stiffness variation of the mechanism. In Section V, a potential application of the variable stiffness mechanism in needle steering is demonstrated by a simple phantom experiment. The stiffness-controlled steerable needle provides an additional degree of freedom to control its trajectory. In Section VI, we discuss the pros and cons of the proposed mechanism and list features needing improvement to derive a more accurate description of the characteristics of varying stiffness effects of the mechanism.
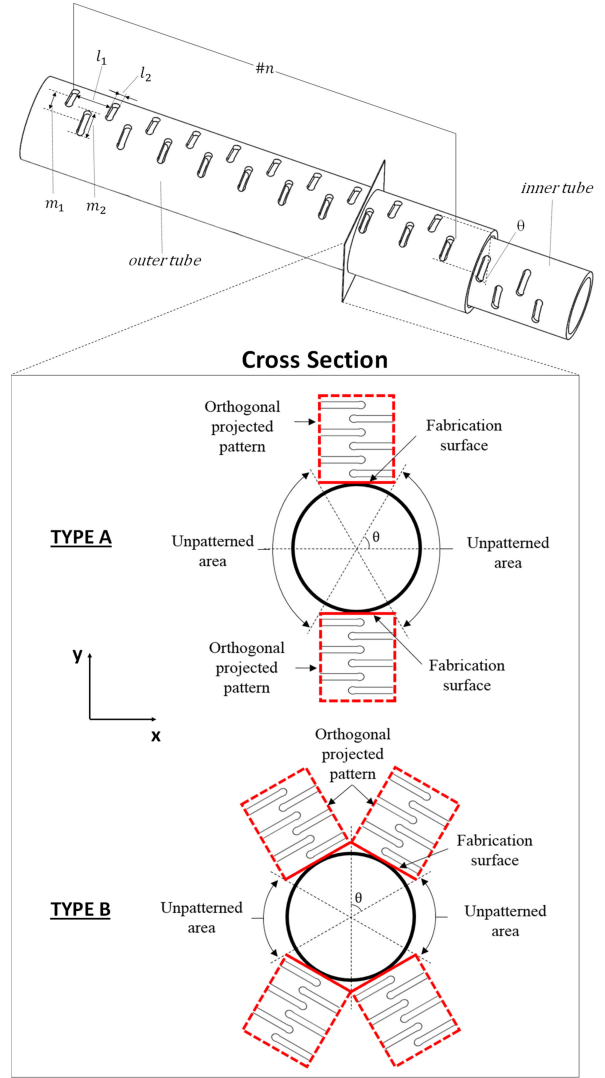

Fig. 1. Design parameters of nonuniform pattern: $(l_1, l_2, m_1, m_2, \theta, n)$. The cross-sectional view shows how the through-hole patterns are engraved on the tubes of types A and B.

II. DESIGN AND MODELING OF THE MECHANISM

A. Concept and Design of the Mechanism

The proposed variable stiffness mechanism consists of two or more coaxial tubes with nonuniform through-hole patterns as shown in Fig. 1. The cross section of the tube consists of arc-shaped units with (shaded) and without (unshaded) patterns as shown in Fig. 2. Averaging along the longitudinal direction, the patterning has an effect of decreasing the flexural stiffness (EI) of the unit, leading to the anisotropic distribution of the flexural stiffness (EI) within its cross sections. As a result, the flexural stiffness of the tube with respect to the fixed load direction changes with the rotation of the tube.

The pattern design parameters determine the stiffness range–m_1 and l_1 are the radial and the longitudinal distance between the patterns, respectively; m_2 and l_2 stand for width and height of a unit pattern, respectively; θ for the angle of the arc unit; n for the number of units.

This article has been accepted for inclusion in a future issue of this journal. Content is final as presented, with the exception of pagination.

KIM *et al.*: CONTINUOUSLY VARIABLE STIFFNESS MECHANISM USING NONUNIFORM PATTERNS ON COAXIAL TUBES
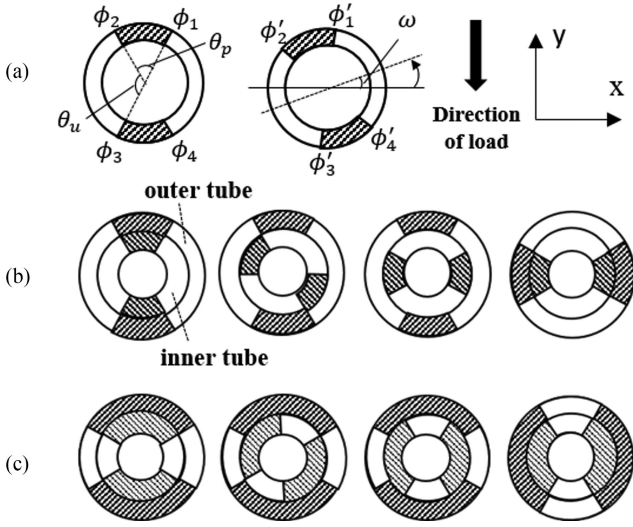
3

Fig. 2. (a) Cross section of the single-patterned tube at the initial state (left) and rotated by ω from the initial state (right). The relative rotational configuration brings variable stiffness. (ω_1, ω_2) is an element of $\{(0°, 0°), (60°, 0°), (90°, 0°), (90°, 90°)\}$ from the left when ω_1 and ω_2 are the rotational angles for inner and outer tubes, respectively, for (b) Type A and (c) Type B.

TABLE I
SPECIFICATION OF THE INNER AND OUTER TUBES

Tube	d_i (mm)	d_0 (mm)	E (GPa)	l_1 (μm)	l_2 (μm)	m_1 (μm)	m_2 (μm)	θ (°)	n
Outer	1.60	1.80	62.8	250	110	385	372	60	90
Inner	1.27	1.47	60.3	250	110	471	372	60	90

In the previous study [20], the prototype of the mechanism was fabricated with a 3-D printer (Objet Connex 260 Stratasys, USA) with 18 mm diameter. In the prototype, the anisotropic distribution of the flexural stiffness was built by printing each unit with different materials. In this research, to minimize the dimension of the structure and satisfy biocompatibility for applications in minimally invasive surgery, the structure was built using thin nitinol tubes. Nitinol is characterized by biocompatibility, superelasticity, and shape memory effect, and so it is suitable for surgical instruments [21].

To create an anisotropic distribution of flexural stiffness on nitinol tubes, the surface of the tube was partially slit-patterned. We researched various types of patterns and chose a dog-bone-shaped pattern to prevent failure [22]. Two types of nonuniform patterns, types A and B of Fig. 1, were patterned on the tubes for comparison. In type A, one 60° arc unit was patterned on half, and in type B, two 60° arc units were patterned on half. The specification of the inner/outer tube and the design parameters of the pattern are given in Table I. The partial patterning of the tube surface grants nonuniform flexural stiffness to each tube, and the coaxial arrangement of the tubes results in variable stiffness mechanism. Thus, the mechanism does have embodied intelligence that controls variable stiffness by nonuniform flexural stiffness.

TABLE II
STIFFNESS CHANGE ACCORDING TO TRANSLATIONAL CONFIGURATION

State	Relative Translational Configuration
Rigid State	
Flexible State	

B. Variable Stiffness Control: Relative Translational and Rotational Movement Between the Patterned Tubes

There are two major ways to control the stiffness of the mechanism: relative rotational and translational movement between the coaxial tubes. Translating one tube from the other changes the flexural stiffness of the mechanism as shown in Table II. At the flexible state, each patterned segment (the darker segments in Table II) of the inner tube exactly overlaps with that of the outer tube. At the rigid state, each patterned segment of the inner tube positions at the middle of the rigid segment of the outer tube. The rigid segment of the outer tube holds the patterned segment of the inner tube from bending more. To change neighboring segments is the key to achieve variable stiffness in this mechanism. Thus, by translating the inner tube, the mechanism reconfigures from a flexible state to a rigid state.

The other way to control the stiffness is to rotate one tube from the other. The rotational configuration difference also varies the stiffness of the mechanism. In Fig. 2(a), we consider that a tube rotates by ω along counterclockwise from the initial state and dashed area represents a patterned area. The combination of relative translational and rotational motion between the nonuniform tubes provides various stiffness controls in the form of continuous functions rather than discrete ones. This article focuses more on the stiffness variation by relative rotation through modeling, simulation, and experiments.

C. Analytical Modeling of the Stiffness of the Mechanism

The flexural stiffness of the mechanism is a 2×2 symmetric matrix and changes with the rotational angle ω of the inner and outer tubes as in (1). Assume that the tube is radially divided into n sections as shown in Fig 2. If a section is patterned, it has lower flexural stiffness; if unpatterned, it has higher flexural stiffness. The flexural stiffness of the tube can be modeled as the sum of the stiffness of all sections

$$K(\omega) = EI(\omega) = \begin{bmatrix} \sum_{i=1}^{n} (EI_{xx}(\omega))_i & \sum_{i=1}^{n} (EI_{xy}(\omega))_i \\ \sum_{i=1}^{n} (EI_{yx}(\omega))_i & \sum_{i=1}^{n} (EI_{yy}(\omega))_i \end{bmatrix} \quad (1)$$

where $I_{xy} = I_{yx}$, $EI_{xx}(\omega) = EI_{yy}(\omega + \frac{\pi}{2})$, and i indicates the number of sections. Note that I_{xx} is the lowest and I_{yy} is the highest at the initial state like Fig. 2 and $I_{xx}(\omega) = I_{yy}(\omega + \frac{\pi}{2})$. The I_{xy} of the tube is zero at the initial state because it is symmetric to the x-axis.

The flexural stiffness of each section is a product of its second moment of area (I_{xx}, I_{yy}, I_{xy}) and its Young's modulus (E).
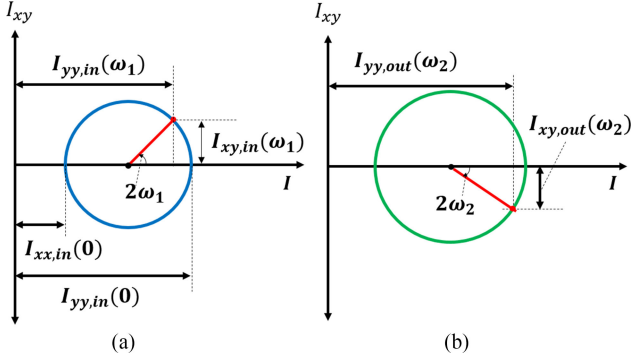
Fig. 3. (a) Mohr's circle (blue) for the inner tube for ω_1. (b) Mohr's circle (green) for the outer tube for ω_2. Notice that $I_{xx}(\omega) = I_{yy}(\omega + \frac{\pi}{2})$.

The second moment of area of the section changes with the rotation of the tube and its variation can be plotted using Mohr's circle as shown in Fig. 3. The reduction of the flexural stiffness by patterning can be modeled as the change of the "effective" Young's modulus of the section.

Each section is either patterned or unpatterned. Let E_p and E_u stand for "effective" Young's modulus of the patterned and unpatterned sections, respectively. The effective Young's modulus is defined by the averaging Young's modulus over the longitudinal length of the section. The effective Young's modulus E_u was measured by the three-point bending test for the given nitinol tube as in Table I; E_p was measured by the three-point bending test for the 360° patterned nitinol tube. The measured values E_p for the outer tube and the inner tube are 6.3 and 6.0 GPa, respectively. Alternatively, in the previous study [23], based on the design variables of the pattern, we constructed a lumped analysis model of the effective Young's modulus of the patterned.

At first, consider K_{xx} when ω is zero; r_o and r_i are the outer and the inner radius of the tube, respectively.

$$
\begin{aligned}
K_{xx}(0) &= \sum_{i=1}^{n} (EI_{xx}(0))_i \\
&= (EI_{xx}(0))_1 + (EI_{xx}(0))_2 + \cdots \\
&\quad + (EI_{xx}(0))_{n-1} + (EI_{xx}(0))_n \\
&= E_1(I_{xx}(0))_1 + \cdots + E_{n-1}(I_{xx}(0))_{n-1} \\
&\quad + E_n(I_{xx}(0))_n \\
&= E_p \int_{r_i}^{r_o} \int_{\phi_1}^{\phi_2} (r\sin\theta)^2 r\,d\theta\,dr \\
&\quad + E_u \int_{r_i}^{r_o} \int_{\phi_2}^{\phi_3} (r\sin\theta)^2 r\,d\theta\,dr \\
&\quad + E_p \int_{r_i}^{r_o} \int_{\phi_3}^{\phi_4} (r\sin\theta)^2 r\,d\theta\,dr \\
&\quad + E_u \int_{r_i}^{r_o} \int_{\phi_4}^{\phi_1+2\pi} (r\sin\theta)^2 r\,d\theta\,dr \quad (2)
\end{aligned}
$$

where

$$
\phi_2 = \phi_1 + \theta_p, \phi_3 = \phi_1 + \pi, \phi_4 = \phi_1 + \pi + \theta_p. \quad (3)
$$

Define $G(\phi', \phi, r_o, r_i)$ as

$$
\begin{aligned}
G(\phi', \phi, r_o, r_i) &= \int_{r_i}^{r_o} \int_{\phi}^{\phi'} (r\sin\theta)^2 r\,d\theta\,dr \\
&= \int_{r_i}^{r_o} \int_{\phi}^{\phi'} r^3\sin^2\theta\,d\theta\,dr = \frac{r_o{}^4 - r_i{}^4}{4} \int_{\phi}^{\phi'} \sin^2\theta\,d\theta \\
&= \left(\frac{r_o{}^4 - r_i{}^4}{4} \right) [(\phi' - \phi) - \sin(\phi' - \phi)\cos(\phi' + \phi)].
\end{aligned}
$$
(4)

Using (4), solve (2)

$$
\begin{aligned}
K_{xx}(0) &= E_p\, G(\phi_1, \phi_2, d_o, d_i) \\
&\quad + E_u G(\phi_2, \phi_3, d_o, d_i) + E_p\, G(\phi_3, \phi_4, d_o, d_i) \\
&\quad + E_u\, G(\phi_4, \phi_1 + 2\pi, d_o, d_i) \\
&= \left(\frac{r_o{}^4 - r_i{}^4}{4} \right) [E_p(2\theta_p - 2\sin\theta_p\cos(2\phi_1 + \theta_p)) \\
&\quad + E_u(2\pi - 2\theta_p + 2\sin(\theta_p)\cos(2\phi_1 + \theta_p))] \quad (5)
\end{aligned}
$$

For type A, as $\phi_1 = \frac{\pi}{3}$ and $\theta_p = \frac{\pi}{3}$, (5) becomes

$$
K_{A\_xx}(0) = \left(\frac{r_o{}^4 - r_i{}^4}{4} \right) \left[E_p\left(\frac{2\pi}{3} + \sqrt{3} \right) + E_u\left(\frac{4\pi}{3} - \sqrt{3} \right) \right]. \quad (6)
$$

Similarly,

$$
K_{A\_yy}(0) = \left(\frac{r_o{}^4 - r_i{}^4}{4} \right) \left[E_p\left(\frac{2\pi}{3} - \sqrt{3} \right) + E_u\left(\frac{4\pi}{3} + \sqrt{3} \right) \right]. \quad (7)
$$

For type B, as $\phi_1 = \frac{\pi}{6}$ and $\theta_p = \frac{2\pi}{3}$, (5) becomes

$$
K_{B\_xx}(0) = \left(\frac{r_o{}^4 - r_i{}^4}{4} \right) \left[E_p\left(\frac{4\pi}{3} + \sqrt{3} \right) + E_u\left(\frac{2\pi}{3} - \sqrt{3} \right) \right] \quad (8)
$$

$$
K_{B\_yy}(0) = \left(\frac{r_o{}^4 - r_i{}^4}{4} \right) \left[E_p\left(\frac{4\pi}{3} - \sqrt{3} \right) + E_u\left(\frac{2\pi}{3} + \sqrt{3} \right) \right]. \quad (9)
$$

The change of the flexural stiffness due to the rotation of the tube can be calculated by the transformation law of the flexural stiffness tensor. When R represents the rotational matrix by ω, the 2-by-2 flexural stiffness, $K(\omega)$ is determined by (10).

$$
K(\omega) = RK(0)R^T \quad (10)
$$

This article has been accepted for inclusion in a future issue of this journal. Content is final as presented, with the exception of pagination.

KIM *et al.*: CONTINUOUSLY VARIABLE STIFFNESS MECHANISM USING NONUNIFORM PATTERNS ON COAXIAL TUBES 5

$$\begin{bmatrix} K_{xx}(\omega) & K_{xy}(\omega) \\ K_{yx}(\omega) & K_{yy}(\omega) \end{bmatrix}$$

$$= \begin{bmatrix} \cos(\omega) & \sin(\omega) \\ -\sin(\omega) & \cos(\omega) \end{bmatrix} \begin{bmatrix} K_{xx}(0) & 0 \\ 0 & K_{yy}(0) \end{bmatrix}$$

$$\begin{bmatrix} \cos(\omega) & -\sin(\omega) \\ \sin(\omega) & \cos(\omega) \end{bmatrix}$$

$$= \begin{bmatrix} \cos^2(\omega)K_{xx}(0) + \sin^2(\omega)K_{yy}(0) \\ \cos(\omega)\sin(\omega)\left(K_{yy}(0) - K_{xx}(0)\right) \\ \cos(\omega)\sin(\omega)\left(K_{yy}(0) - K_{xx}(0)\right) \\ \sin^2(\omega)K_{xx}(0) + \cos^2(\omega)K_{yy}(0) \end{bmatrix}. \quad (11)$$

$K_{xx}(0)$ and $K_{yy}(0)$ are calculated in (6)–(9), and the 2-by-2 flexural stiffness can be determined by (11). Expanding (11) for type A

$$K_{xx}(\omega) = \cos^2(\omega)K_{xx}(0) + \sin^2(\omega)K_{yy}(0)$$

$$= \left(\frac{r_o{}^4 - r_i{}^4}{4}\right)\left[E_p\left(\frac{2\pi}{3} + \sqrt{3}\cos 2\omega\right)\right.$$

$$\left. + E_u\left(\frac{4\pi}{3} - \sqrt{3}\cos 2\omega\right)\right] \quad (12)$$

$$K_{xy}(\omega) = K_{yx}(\omega) = \cos(\omega)\sin(\omega)\left(K_{yy}(0) - K_{xx}(0)\right)$$

$$= \left(\frac{r_o{}^4 - r_i{}^4}{4}\right)\cos(\omega)\sin(\omega)\left[E_p\left(-2\sqrt{3}\right) + E_u\left(2\sqrt{3}\right)\right] \quad (13)$$

$$K_{yy}(\omega) = \sin^2(\omega)K_{xx}(0) + \cos^2(\omega)K_{yy}(0)$$

$$= \left(\frac{r_o{}^4 - r_i{}^4}{4}\right)\left[E_p\left(\frac{2\pi}{3} + \sqrt{3}(\cos(2\omega - \pi))\right)\right.$$

$$\left. + E_u\left(\frac{4\pi}{3} - \sqrt{3}(\cos(2\omega - \pi)\right)\right]. \quad (14)$$

Similarly, the flexural stiffness for type B can be calculated. Notice (3), and it is enough to study for $0 \leq \omega \leq \frac{\pi}{2}$ because the pattern is symmetric with respect to the origin of the tube's circle at the cross section. The flexural stiffness of the multiple tube structure is the summation of those of the single tubes.

In Fig. 4, we plotted the change of the flexural stiffness K_{xx} of the double tube mechanism of types A and B based on (12)–(14). As the rotational angle changes from 0° to 90°, the figures show the change of the flexural stiffness ratio. The flexural stiffness was found to increase in the order of $(0°, 0°)$, $(60°, 0°)$, $(90°, 0°)$, and $(90°, 90°)$ as illustrated in Fig. 2(b) and (c). The maximum difference is 2.10 times for type A and 4.27 times for type B. The detailed results are summarized in Table III.

D. Decoupling I_{xx} and I_{xy}

In Fig. 3, Mohr's circle demonstrates the relationship between I_{xx} and I_{xy} for the rotational angle ω as (15).

$$\left(\frac{I_{yy}(0) - I_{xx}(0)}{2}\right)^2$$

$$= (I_{xy}(\omega))^2 + \left(\frac{2I_{yy}(\omega) - I_{yy}(0) + I_{xx}(0)}{2}\right)^2. \quad (15)$$
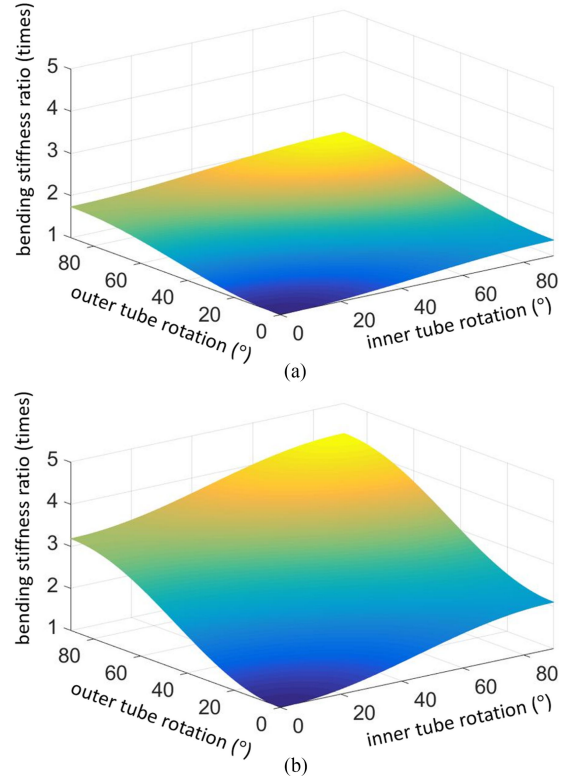

(a)

(b)

Fig. 4. As the inner and outer tubes rotate, the graph describes the change in the flexural stiffness (K_{xx}) ratio of (a) Type A and (b) Type B structure according to the analytical modeling.

TABLE III
BENDING STIFFNESS CHANGE AND ITS RATIO (TIMES) COMPARISON

	ω_1, ω_2	K_{xx} ($kNmm^2$)		
		Analytic Modeling	FEM Simulation	3pt Bending Experiment
Type A	0°, 0°	16.6 (1.00)	15.6 (1.00)	14.4 (1.00)
	60°, 0°	21.1 (1.27)	18.6 (1.19)	16.6 (1.16)
	90°, 0°	22.6 (1.37)	20.1 (1.29)	18.6 (1.30)
	90°, 90°	34.7 (2.10)	31.5 (2.02)	33.4 (2.33)
Type B	0°, 0°	5.61 (1.00)	7.07 (1.00)	5.12 (1.00)
	60°, 0°	10.2 (1.81)	11.3 (1.60)	8.83 (1.72)
	90°, 0°	11.7 (2.08)	12.2 (1.74)	10.5 (2.05)
	90°, 90°	23.7 (4.23)	22.0 (3.12)	22.7 (4.44)

The single tube rotation have coupled I_{xx} and I_{xy}. In other words, not only I_{xx} but also I_{xy} varies simultaneously while the tube rotates. When I_{xy} is not zero, the structure has out-of-plane deflection to the load, resulting in undesired motion. To cancel out I_{xy}, the counterrotation of the outer tube is utilized. For instance, the inner tube's rotation is given with $I_{xy, \text{in}}$. Then, one

This article has been accepted for inclusion in a future issue of this journal. Content is final as presented, with the exception of pagination.

6   IEEE TRANSACTIONS ON ROBOTICS

is always possible to have ω_2 to satisfy (16) when the radius of the outer tube's Mohr's circle is the same or larger than that of the inner.

$$I_{xy,\text{in}}(\omega_1) + I_{xy,\text{out}}(\omega_2) = 0. \tag{16}$$

In other words, in contrast to the single-tube mechanism, the multiple-tube mechanism enables decoupling I_{xx} and I_{xy}, and it controls both independently. It explains why the multiple tubes are required to prevent out-of-plane deflection to load. In double-tube structure, if we design the Mohr's circle of the inner and the outer tubes to have the same radius, it achieves continuously variable stiffness of K_{xx} for all stiffness range while keeping $K_{xy} = 0$. To have the same radius of Mohr's circle for both tubes, (17) should be satisfied.

$$\left(\frac{K_{yy}(0) - K_{xx}(0)}{2}\right)_{\text{inner}} = \left(\frac{K_{yy}(0) - K_{xx}(0)}{2}\right)_{\text{outer}}. \tag{17}$$

Considering (6)–(9), (17) becomes (18). It means that θ_p for the outer tube should be larger than that of the inner tube to satisfy (17) because the radius of the inner tube is smaller than that of the outer tube.

$$\frac{R_o^4 - R_i^4}{r_o^4 - r_i^4} = \frac{E_{p,\text{in}} - E_u}{E_{p,\text{out}} - E_u} \tag{18}$$

where R_o and R_i stand for the outer and inner radius of the outer tube, respectively; subscripts "in" and "out" represent the inner tube and the outer tube, respectively. When the radii of Mohr's circle are the same each other, ω_1 is simply equal to $-\omega_2$ to satisfy (16). Alternatively, the structure is able to consist of three or more coaxial tubes to control I_{xx} and I_{xy} independently.

E. Pattern Design to Customize the Stiffness Range

Set the ratio of $K_{xx}(90°)$ to $K_{xx}(0°)$ to compare the maximum and minimum stiffness of a single tube. Using (12) and $\phi_1 = \frac{\pi - \theta_p}{2}$ in our design as Fig. 2, the ratio becomes (19).

$$
\begin{aligned}
K_{xx\_ratio} &= \frac{K_{xx}(90°)}{K_{xx}(0°)} \\
&= \frac{(2\theta_p - 2\sin\theta_p) + (E_u/E_p)(2\pi - 2\theta_p + 2\sin\theta_p)}{(2\theta_p + 2\sin\theta_p) + (E_u/E_p)(2\pi - 2\theta_p - 2\sin\theta_p)}.
\end{aligned} \tag{19}
$$

It means the ratio is the function of the central angle for the patterned area, θ_p and E_u/E_p. The value E_u/E_p is determined by the pattern shape. Fig. 5 demonstrates the variation of stiffness ratio for $0° \leq \theta_p \leq 180°$ where E_u/E_p are given according to our pattern design. In the result, the ratio shows the maximum value, 4.378 times at $\theta_p = 128.9°$. The angle of the patterned area for the maximum ratio depends on the value of E_u/E_p. On the other hand, it is trivial that the ratio has the minimum value of 1 at $\theta_p = 0°$ and $180°$. Thus, by tuning θ_p and E_u/E_p, we can optimize the desired range of the stiffness.

Also, we set the ratio of $EI(90°, 90°)$ to $EI(0°, 0°)$ to compare the maximum to the minimum stiffness of the double-tube
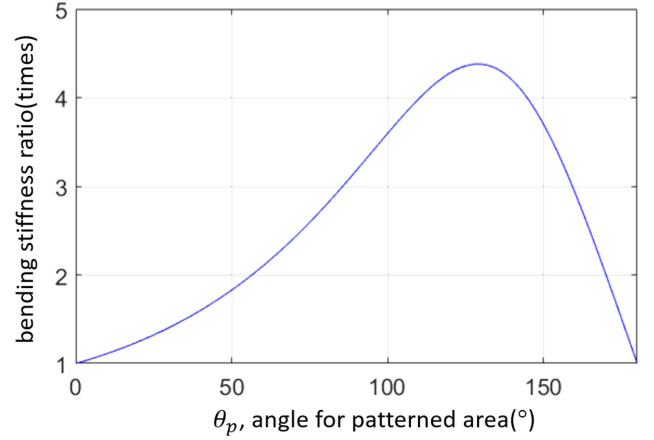

Fig. 5.   Bending stiffness ratio of a single-patterned tube according to the angle for the patterned area, θ_p. The ratio is maximum when $\theta_p = 128.9°$.

mechanism as (20).

$$\frac{EI(90°, 90°)}{EI(0°, 0°)} = \frac{EI(90°)_{\text{inner}} + EI(90°)_{\text{outer}}}{EI(0°)_{\text{inner}} + EI(0°)_{\text{outer}}}. \tag{20}$$

Let t be the thickness of the tube, then $d_i = d_o - 2t$. $d_i^4 = (d_O - 2t)^4 = d_o^4 - 2td_o^3 + 4t^2d_o^2 - 8t^3d_o + 16t^4 \approx d_o^4 - 2td_o^3$. When t_i and t_o are the thickness of the inner and outer tubes, respectively, expand (20) to (21).

$$
\begin{aligned}
(1/64)&(t_i{d_o}^3[E_{p\_i}(2\theta_p - 2\sin\theta_p) \\
&+ E_{u\_i}(2\pi - 2\theta_p + 2\sin\theta_p)] + t_o{D_o}^3[E_{p\_o}(2\theta_p - 2\sin\theta_p) \\
&+ E_{u\_o}(2\pi - 2\theta_p + 2\sin\theta_p)]) \div (t_i{d_o}^3[E_{p\_i}(2\theta_p + 2\sin\theta_p) \\
&+ E_{u\_i}(2\pi - 2\theta_p - 2\sin\theta_p)] + t_o{D_o}^3[E_{p\_o}(2\theta_p + 2\sin\theta_p) \\
&+ E_{u_o}(2\pi - 2\theta_p - 2\sin\theta_p)]).
\end{aligned} \tag{21}
$$

Finally, (21) shows that the stiffness ratio is determined by the tube dimension, pattern shape, and the angle for the patterned area, θ_p. The relationship helps to establish the stiffness range of the mechanism to fulfill target requirements.

III. FINITE ELEMENT METHOD SIMULATION

To verify the variation of the stiffness predicted from the model, three-point bending test like Fig. 6(a) was simulated for different relative rotations between the coaxial tube sets. The FEM simulation was performed using Abaqus 6.14. (Dassault Systèmes, Vélizy-Villacoublay, France). There is a study to perform finite-element method (FEM) simulation on superelastic nitinol [24]. Since the sample and the load are symmetric with respect to the middle point, only half of the three-point bending point test was simulated as in Fig. 6(c) to reduce the computational load.

In the FEM simulation, the middle point was displaced 2 mm downwards and the bearings had surface-to-surface contact with the coaxial tube structure. The length between the two lower supporters is 40 mm. Force–displacement relationship of the middle point was computed. The simulation was performed for the selected configurations shown in Fig. 2(b) and (c) of {(0°,

This article has been accepted for inclusion in a future issue of this journal. Content is final as presented, with the exception of pagination.

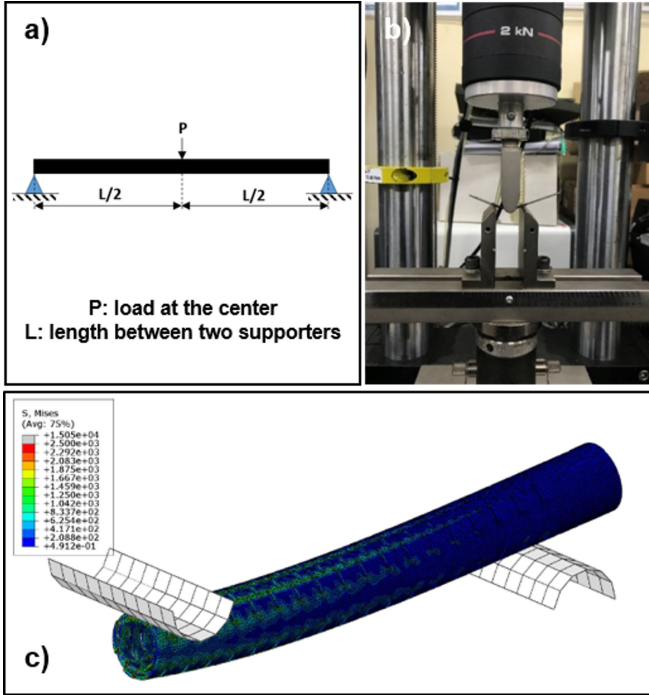KIM *et al.*: CONTINUOUSLY VARIABLE STIFFNESS MECHANISM USING NONUNIFORM PATTERNS ON COAXIAL TUBES

7

Fig. 6. Three-point bending test by (a) the diagram, (b) the experimental setups using Instron 5900 series, and (c) FEM simulation by Abaqus 6.14.

Fig. 7. FEM simulation results of Type A (upper) and Type B (lower) structure when $(\omega_1, \omega_2) \in \{(0°, 0°), (60°, 0°), (90°, 0°), (90°, 90°)\}$.

0°), (60°, 0°), (90°, 0°), (90°, 90°)} for types A and B. The load–deflection relationships are plotted in Fig. 6. The flexural stiffness was calculated by fitting the linear trend line to the load–deflection curve and substituting the slope of the trend line into (12). In Fig. 7, the flexural stiffness was found to increase in the order of (0°, 0°), (60°, 0°), (90°, 0°), and (90°, 90°). The results are listed in Table III.

IV. FABRICATION AND EXPERIMENT

The through-hole patterns were engraved on the nitinol tube by nanosecond UV laser machining. To verify the stiffness variability of the mechanism and the feasibility of the model, the variation of the flexural stiffness predicted from the model in Section II and simulation in Section III was compared with the experimental results. Then, we set up a robotic system to control the stiffness of the mechanism. Using the system, continuous variation of the stiffness was demonstrated by a simple load test. Also, an experiment on the potential application of the mechanism in stiffness-controlled needle steering was performed.

A. Ultraviolet Laser Machining

Based on the proposed mechanism, the tubes should have nonuniform flexural stiffness to accomplish variable stiffness. We engraved patterns on the nitinol tubes by ultraviolet (UV) laser. Owing to its mechanical strength, superelasticity, and excellent biocompatibility, nitinol is regarded as an outstanding material for biomedical applications, and intensive study of nitinol fabrication has been conducted [25], [26]. In our study,
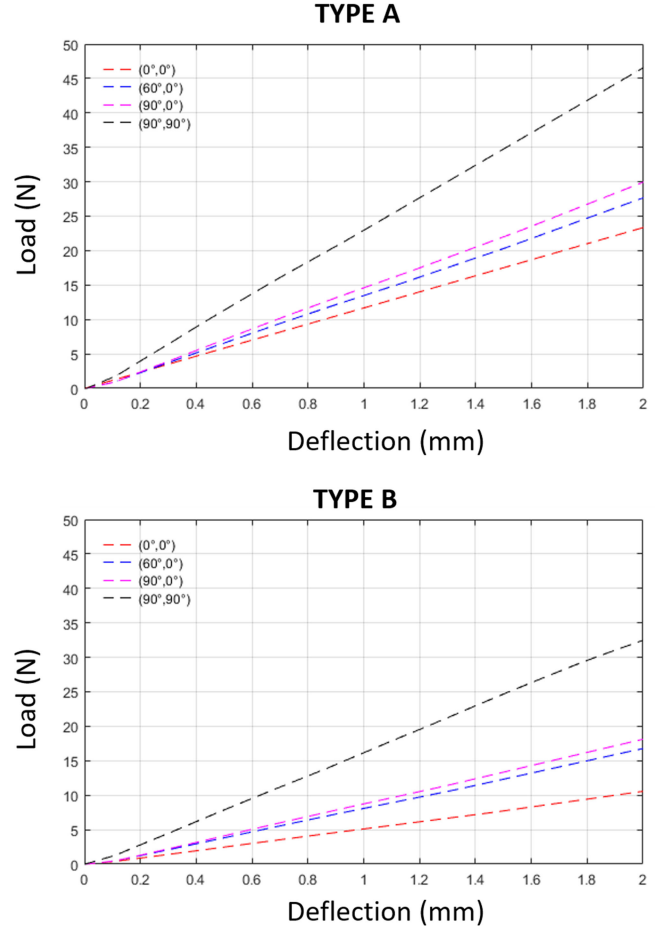
we employed Nd:YVO$_4$ laser system (wavelength of 355 nm, linewidth of 20 μm, pulse duration of 30 ns, the repetition rate of 100 kHz) to engrave the patterns on the tubes. Due to the surface curvature of the tubes, the maximum cutting depth of the tube was approximately 150 μm with a maximum laser power of 3.1 W, scanner speed of 40 mm/s, and 50 repetitions.

The desired pattern, illustrated in Fig. 1, spanned the tube's surface along the radial and axial directions. A specialized system was required to cut the pattern into the curved surface with minimum distortion. Ideally, the rotation of the tube would be synchronized with the laser scanner movement to allow for continuous patterning along the perimeters of the tube, but this is technically demanding. To simplify the procedure while minimizing the error caused by the curvature of the tube surface, the surface of the tube was divided into six equal regions and each region was patterned at a time. The tube was then rotated 60° and patterned again, for a total of two (type A) or four (type B) processing repeats according to its design. The surface can be divided into smaller regions depending on the pattern design. Also, the cooling system and enough cooling time reduce the heat effect near laser-engraving spots.

Fig. 8(a) demonstrates the machining setup for the tubes. A rotary motor stage (Unice E-O Service Inc., Taiwan) was installed
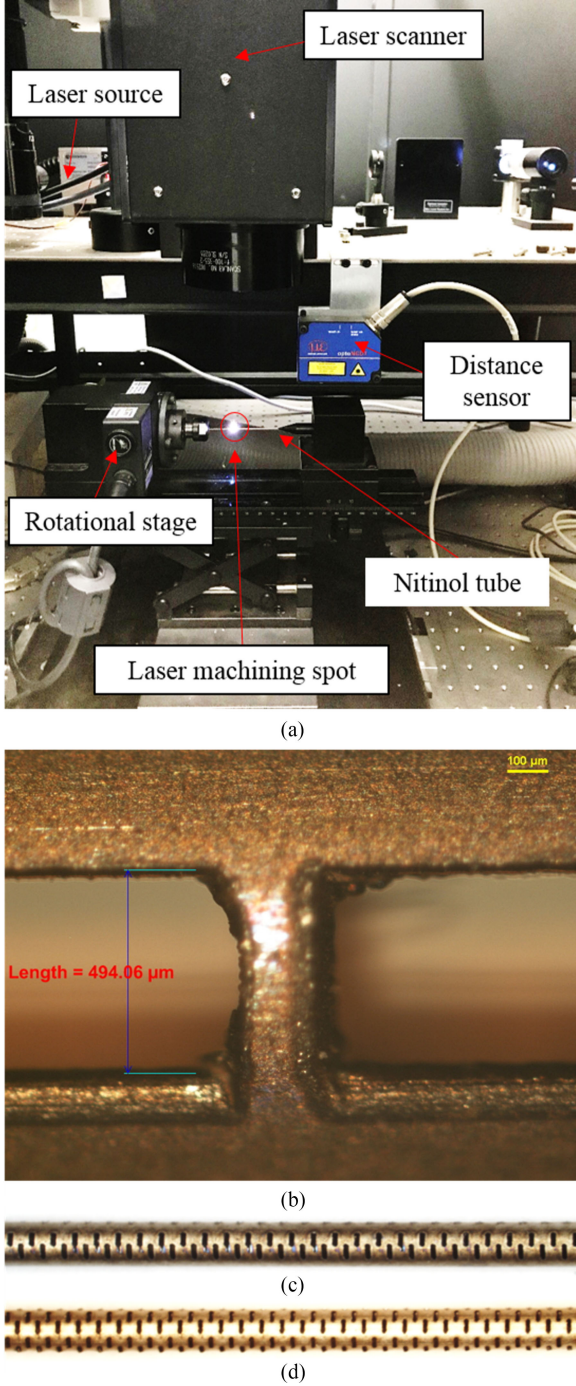
(a)

(b)

(c)

(d)

Fig. 8.   (a) UV laser machining setups. (b) Enlarged image of the engraved tube surface. (c) Laser-patterned nitinol tube for Type A and (d) Type B.

to rotate the tube precisely. The tube was fixed by a collet chuck, a linear guide set various lengths of the tubes, and a cone-shaped bearing support prevented bending and twisting of the tube. A CCD camera (Color 5MP CMOS camera; Mightex Systems, Pleasanton, CA, USA) was placed above the specimen tube to monitor its dislocations after rotation, and an optoelectronic displacement measurement system (Micro-Epsilon, opto-NCDT 1402) was used to calibrate the vertical position of the tube to

match the focal length of the laser beam. Fig. 8(b) demonstrates the enlarged image of the engraved surface. Due to heat affection, the set up laser system engraves the pattern larger than its original design. Twenty tests confirmed that the length increased by an average of 29 μm over the design. We designed the pattern to compensate for 29 μm to obtain more accurate fabrication results. Fig. 8(c) and (d) shows the fabrication results for types A and B, respectively. Type B has wider patterned area than type A. The pictures were taken by a microscope (SZ61, Olympus, Tokyo, Japan) with a digital camera (acqucam2, jnoptic Company Ltd, Seoul, Korea).

B. Three-Point Bending Test

To experimentally verify the stiffness variation of the mechanism, we performed a bending rigidity test. The result was compared with that from the simulation. The mechanism with two types of pattern, as shown in Figs. 1 and 2, was prepared for bending tests.

The three-point bending method was chosen to examine the bending rigidity of tubes. In this research, we tested specimens with the Instron 5900 series, a high-precision system of measurement. Fig. 6(a) and (b) shows how the bending test setups were installed and a 2 kN load cell was connected. The system measured the applied force and the vertical displacement to calculate the flexural stiffness.

The test was repeated three times per specimen to check its repeatability. The length between the two lower supporters is 38 mm ($L = 38$ mm) and a concentrated load P was applied to the center; I was the second moment of the tube, and ω_0 was the deflection at the center of the tube. Then, the flexural stiffness, (EI), is given by (22), where P/ω_0 is the slope of the load–deflection curve.

$$K_{xx} = EI = \left(\frac{P}{\omega_0}\right)\left(\frac{L^3}{48}\right) \tag{22}$$

For the relative rotational movement, the three-point bending test was performed for each of type A and B. The inner and outer tubes were tested at 0° and 90° to test flexural stiffness. The mechanism was tested for the selected configurations of Fig. 2(b) and (c), where (ω_1, ω_2) is an element of {(0°, 0°), (0°, 60°), (0°, 90°), (90°, 90°)} and the results are shown in Fig. 9. The load–deflection curve for each test was obtained in the three-point bending test. The flexural stiffness was calculated by fitting the linear trend line to the load–deflection curve and substituting the slope of the trend line into (22). As with the analytical modeling results, type B exhibits more changes in flexural stiffness than type A; type A showed the 2.17 times difference and type B showed 4.44 times difference. The detailed results are summarized in Table III.

C. Comparison of the Flexural Stiffness Change

We obtained the flexural stiffness of the mechanism through analytical modeling, FEM simulation, and three-point bending experiments. For all three methods, the flexural stiffness changes when (ω_1, ω_2) is an element of {(0°, 0°), (0°, 60°), (0°, 90°), (90°, 90°)}, and are compared in Table III. In the table, the

This article has been accepted for inclusion in a future issue of this journal. Content is final as presented, with the exception of pagination.

KIM *et al.*: CONTINUOUSLY VARIABLE STIFFNESS MECHANISM USING NONUNIFORM PATTERNS ON COAXIAL TUBES
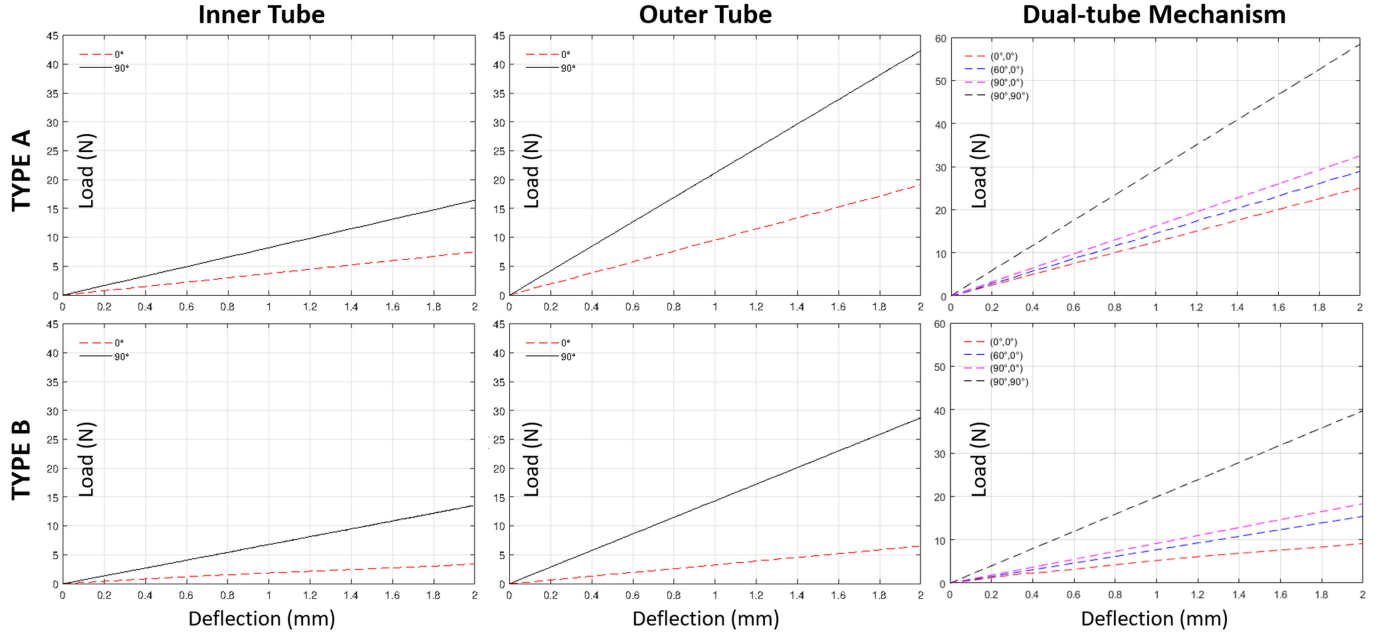
9

Fig. 9. Load–deflection plot from three-point bending experiment. The first and second columns indicate the inner and outer tubes for 0° and 90° rotation. The third column shows the dual-tube mechanism for $(\omega_1, \omega_2) \in \{(0°, 0°), (60°, 0°), (90°, 0°), (90°, 90°)\}$.

value in parenthesis indicates the ratio compared to the value at (0°, 0°). We set the minimum value (0°, 0°) to the standard value and compared the trends of flexural stiffness change. In the results, three methods have the consistency in the tendency of flexural stiffness: the flexural stiffness increases in the order of (0°, 0°), (0°, 60°), (0°, 90°), and (90°, 90°), where (0°, 0°) is the minimum and (90°, 90°) is the maximum. Type B showed more flexural stiffness change compared to type A. Comparing the maximum and minimum experimental values, type A showed 2.10 times increase of stiffness and type B showed 4.23 times for analytical modeling and similar increasing for other methods as Table III. It demonstrates that the range of stiffness is wider as more sections are patterned. Three-point bending experiment results are relatively lower than other results. Overall, the results show the consistency of the trend of stiffness change by all three methods.

D. Demonstration of Continuously Variable Stiffness

A robotic system is built to vary the stiffness of the mechanism. The system has four degrees of freedom: translation along and rotation about the insertion axis for each tube. The collet chucks connected with motors hold the tubes; each tube rotates or translates as each motor operates. The cantilever load test was performed while the stiffness of the mechanism varied. A weight was hung at the distal end of the mechanism and vertical deflection of the distal tip was measured. The flexural stiffness was calculated from the measured deflection. The design parameter of the tube used in the load test was (200 μm, 400 μm, 800 μm, 1500 μm, 60°, 90) of type B patterning. Fig. 10 compares deflections and flexural stiffness when 10 and 20 g loads are applied to the mechanism with different rotational configurations $(\omega_1, \omega_2) = (0, 0), (90, 90)$.
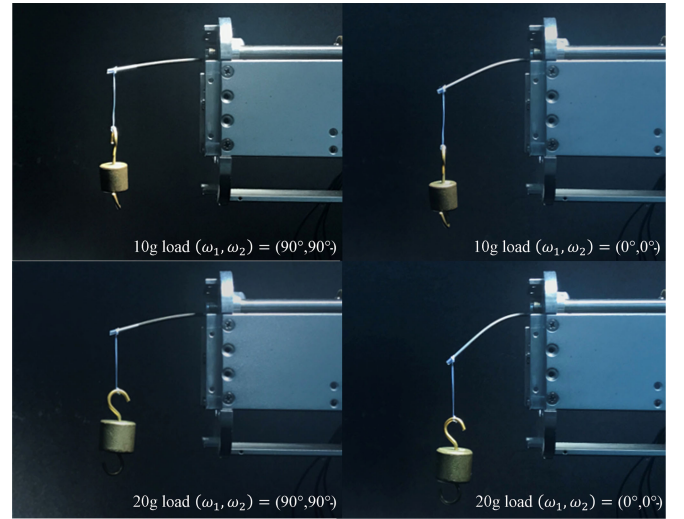

Fig. 10. Cantilever load test was performed for the variable stiffness structure. The tip position demonstrated continuous deflections while both the inner and outer tubes had rotational angles varying with continuous sinusoidal wave.

The deflection at (0, 0) is the maximum while that of (90, 90) is the minimum. The flexural stiffness increases from 1490.8 to 10766 Nmm^2 (about 7.2 times) when (0, 0) and (90, 90) are compared. The complimentary video shows the change of deflection while both the inner and outer tubes have rotational angles that vary with a continuous sinusoidal wave. It demonstrates the continuously variable stiffness change by relative rotational movement. Additionally, the response time is only a few microseconds as the motors directly rotate the coaxial tubes. In the experiment, snapping is not observed. In addition, using a counterrotation method introduced in Section II-D, we

This article has been accepted for inclusion in a future issue of this journal. Content is final as presented, with the exception of pagination.

10   IEEE TRANSACTIONS ON ROBOTICS
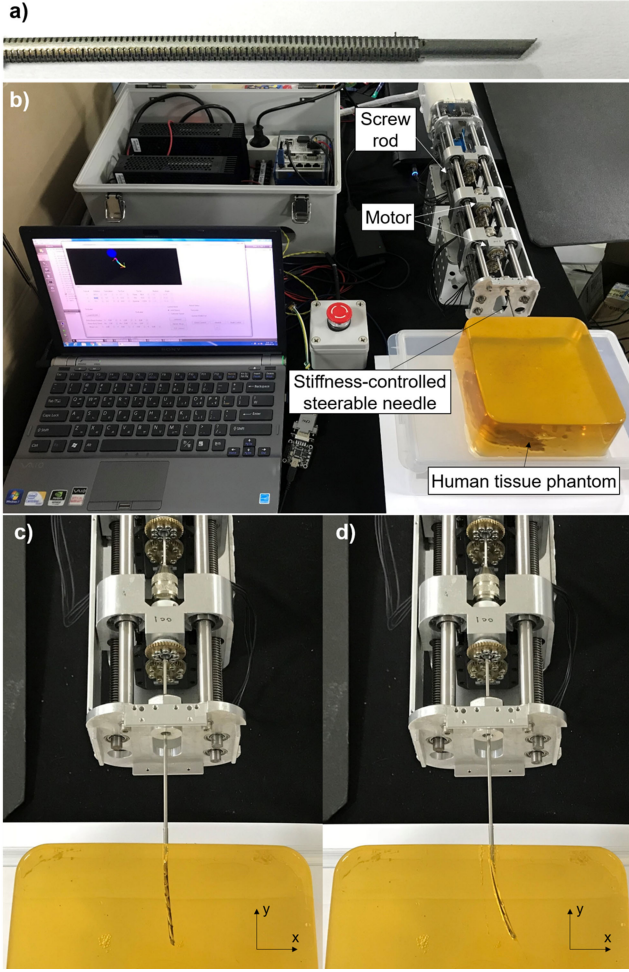

Fig. 11.   (a) Stiffness-controlled steerable needle consists of the bevel-tip inner tube and the nonuniform patterned outer tube. (b) Experimental setups for the insertion of the stiffness-controlled steerable needle. The comparison of the needle's distal tip position at (c) $(\omega_1, \omega_2) = (0, \ 90)$ and (d) $(0, \ 0)$.
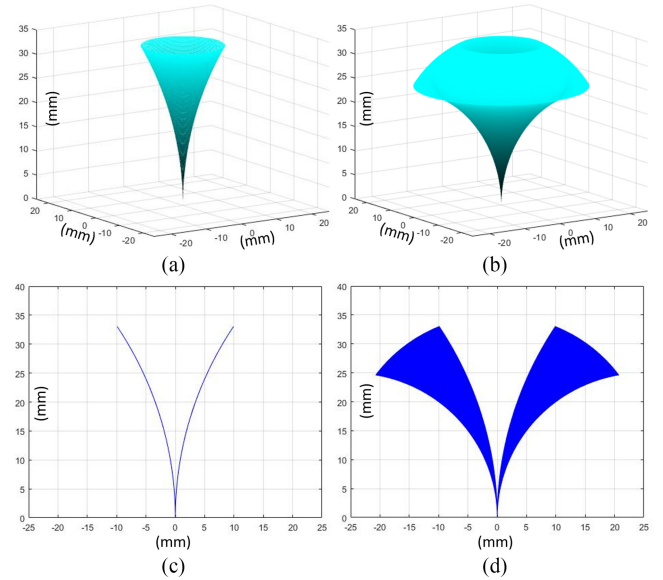

Fig. 12.   Workspace comparison between (a) the needle with constant insertion speed and (b) the stiffness-controlled needle with the constant insertion speed. (c) and (d) Cross section of (a) and (b), respectively.

observed that the out-of-plane deflection is negligible (less than a few tens of micrometers).

V. STIFFNESS-CONTROLLED STEERABLE NEEDLE

One of the possible applications of the mechanism is steering bevel-tip needle. As a flexible needle with a bevel tip is pushed through soft tissue, the asymmetry of the tip causes the needle to bend. The tissue imposes a reaction force on the bevel that deflects the needle tip, causing it to follow an arc [27], [28]. As our variable stiffness mechanism enables the steerable needles to change its directional flexural stiffness, it can control the curvature of the bending, and, in other words, vary the radius of the arc that needle follows. Thus, the mechanism grants additional input to the steerable needle system. We proceeded the demo test to control the curvature of the needle using the mechanism.

The experimental setup used for inserting a stiffness-controlled steerable needle into phantom tissue is shown in Fig. 11(a) and (b). The inner tube has a bevel tip of 45 degrees

at the distal end and uniformly patterned. The outer tube is nonuniform patterned as type B. Alternatively, the needle can consist of a bevel-tipped outer tube and a nonuniform patterned inner tube. It is also possible to have three or more coaxial tubes.

The controller controls the 2R-2T motion of the steerable needle. The rotational and translational movement of each tube (the inner and the outer) is controlled independently. The rotational movement is controlled by Dynamixel using CAN communication and the translational movement is controlled by Maxon motor using RS-485 communication. Each Maxon motors' rotational movement transits into translational movement through lead screw while Dynamixel rotates each tube held by collet chuck. Telecentric lens or camcorder is set to capture the motion of the distal tip of the needle. The phantom tissue is prepared with elastic properties similar to human tissues [29]. The needle is inserted in the homogenous phantom prepared with a mixture of 83% water, 12% gelatin, and 5% sugar. The control system with four degrees of freedom inserts the needle with a velocity of 1 mm/s and the needle stops when inserted 50 mm. For the rotational configurations of $(0, \ 0)$ and $(0, \ 90)$, the needle was inserted into the phantom and the position of the distal tip compared. The needle tip deflected 11.6 mm along x-direction at $(0, \ 0)$ while it deflected 3.5 mm along x-direction at $(0, \ 90)$ from the insertion point as illustrated in Fig. 11(c) and (d). The radii of curvature are 89.7 and 327 mm for $(0, \ 0)$ and $(0, \ 90)$, respectively. The complementary video shows how the needle bends depending on its stiffness. The smaller the stiffness of the mechanism is, the smaller the radius of curvature of the arc that needle follows becomes.

Thus, the variable stiffness mechanism adds an additional degree of freedom to control the trajectory of the needle. The current steerable needles use insertion speed change [30] or duty-cycle method [31] to change its curvature of trajectory.

Moreover, the results demonstrate that the proposed variable stiffness mechanism allows an additional degree of freedom (DOF) to change the radius of curvature. With the additional DOF, the reachable area of the steerable needle can be expanded while keeping its insertion and rotation speed low.

The difference of the workspace of constant insertion speed needle (case **ii**) and constant insertion speed needle with stiffness control (case **i**) is simulated in Fig. 12. In both cases, the insertion speed was constant and the bevel tip tube does not rotate after insertion started. In case **i**, the radius of curvature was fixed to 60 mm due to constant stiffness, and in case **ii**, the radius of curvature was variable from 25 to 60 mm due to variable stiffness. For both cases, the needles are inserted for 35 mm. Case **i** has the cone-like shell workspace with 9.92 mm radius while case **ii** has the thick cone-like workspace with the radius from 9.92 to 20.75 mm like Fig. 12(a) and (b), respectively. The cross section of the case **i**'s workspace is only two curved lines while that of case **ii**'s workspace has a wider area as illustrated in Fig. 12(c) and (d). Thus, the proposed variable stiffness mechanism expands the workspace of the steerable needle, and it can also be applied together with current control methods [30]–[32].

VI. DISCUSSION

In this article, we presented a mechanism for varying the stiffness of a tubular structure by relative rotation and translation among a set of tubes with the anisotropic distribution of the flexural stiffness (EI). In the presented mechanism, the anisotropy is created by machining through-hole patterns on selected surfaces of the nitinol tubes. Alternatively, it is able to use localized annealing to induce the phase transition of nitinol from martensite to austenite. In the research, to have a bigger difference in flexural stiffness, the variable stiffness is primarily achieved by material removal rather than phase transition.

An analytical model was formulated that describes the change in stiffness as a function of rotation of two coaxial tubes. Also, the relationship between the design parameters and the range of stiffness variation was modeled. Using the relationship in (6)–(21), design parameters can be selected to adjust the range of stiffness variation according to target applications.

The directional flexural stiffness of the mechanism is a continuous function of relative rotational angle and translational displacements between the tubes. This characteristic is distinguished from other previous variable stiffness mechanisms with binary or discrete stiffness control. The flexural stiffness of the mechanism can be set to any values between the maximum (90°, 90°) and the minimum (0°, 0°) through the relative rotation between two coaxial tubes. The load test demonstrates the continuously variable stiffness of the mechanism.

Furthermore, embodied intelligence of the mechanism leads to a simple and scalable structure. The mechanism only consists of two coaxial tubes without any bulky or complex external connections such as pneumatic lines or heating wires. Therefore, the mechanism is suitable for applications in minimally invasive surgery and can be easily adapted to all types of tube continuum

robot. In this study, we were able to reduce the diameter of the mechanism to 1.8 mm, which is smaller than the current minimally invasive surgical robot generally using 5–20 mm diameter.

Additionally, unlike other variable stiffness mechanisms using heat, electric, and pneumatic stimuli, the response time of the presented mechanism is immediate. The stiffness can be instantly varied by directly translating and rotating the coaxial tubes with motors. Fast response times are very useful in reducing operative time and in responding to immediate surgical conditions and intuitive control of operators.

The proposed mechanism has a relatively narrow range of stiffness variation compared to other mechanisms that utilize phase change materials such as liquid metals. Also, the baseline of the range starts much higher than that using the phase change materials, so the proposed mechanism aims at surgical tasks that require relatively high stiffness. In future work, we will profoundly study the range of stiffness for certain surgical operations in order to adjust the mechanism accordingly.

The variation of the stiffness predicted from the model was verified through three-point bending experiments and FEM simulation. Overall, the model, the experiment, and the simulation showed a consistent tendency of the flexural stiffness change. For type B, the FEM simulation results showed reduced flexural stiffness ratio compared to those of other methods. The FEM simulations demonstrate different results depending on the meshing method, and in terms of simulation, type B is a more complex structure than type A because of the increased number of patterns. This leads to the difficulties of contact constraints and meshing and possibly affects the simulation results.

The error between the modeling and experiments is mainly based on the limit of fabrication. Due to its heat effect, the laser cannot engrave the exact same pattern as its design. Even though we compensated 29 μm to obtain more accurate fabrication results as in Section IV-A, the results still have errors. Because the pattern is micrometric in size, this error is caused by the limitations of the in-house manufacturing process itself. Using more precise machining and systems should reduce the error between theoretical and experimental results. For example, to reduce heat-affected zone and to increase precision, pico or femtosecond UV laser is preferred rather than nanosecond one. In addition, fine finishing and polytetrafluoroethylene (PTFE) coatings reduce friction among the tubes and between the mechanism and contacting tissues.

One of the specific potential applications of the proposed variable stiffness mechanism is needle steering. The preliminary phantom experiment results in this article demonstrate that the curvature of a needle insertion trajectory can be changed by varying the stiffness of the needle using the proposed mechanism. As its stiffness varies continuously, the mechanism grants an additional degree of freedom (DoF) to the steerable needle system to control the curvature of bending.

Currently, the curvature of the steerable needle is controlled by changing the insertion speed [30] or by intermittent rotation of the needle (duty-cycle method) during insertion [31]. The duty-cycle method offers simple and low-cost solutions to control the needle trajectory. Duty-cycle methods using flexure-based tips

This article has been accepted for inclusion in a future issue of this journal. Content is final as presented, with the exception of pagination.

12   IEEE TRANSACTIONS ON ROBOTICS

have also been studied to reduce tissue damage [33]. In addition to the current methods, the steerable needle can provide an additional DoF to control the trajectory of the needle by varying its stiffness with the proposed mechanism. With the cost of an additional actuator to rotate the nonuniform patterned tube, the variable stiffness expands the curvature range of needle's trajectory. The mechanism can also be applied in conjunction with the duty-cycle method. For example, if both intermittent rotation and stiffness control methods are applied, higher curvature can be achieved than if either is applied. In this context, the variable stiffness mechanism can be combined with other methods [30], [31] to have an additional DoF to control the needle's trajectory.

Thanks to the variation of the flexural stiffness, the rotation speed of the bevel-tip tube can be lowered while keeping the same trajectory. Low rotation speed is preferred to reduce friction against surrounding tissue caused by the tube's rotation. Specifically, when the needle consists of a nonpatterned outer tube with a bevel tip and a nonuniform patterned inner tube, the flexural stiffness of the needle is determined by the rotational configuration of the inner tube. As the rotation of the inner tube occurs inside the instrument, the inner tube is not in direct contact with the surrounding tissue.

For future research, we plan to explore the potential benefits of this additional DoF in control of steerable needles. Since it is possible to vary the curvature of trajectory continuously, the stiffness-controlled steerable needle is expected to avoid obstacles and address deeper in more easiness. It is expected to optimize trajectories during various applications such as radiofrequency ablation of liver tumors and prostate brachytherapy. The path-planning method will be studied to avoid obstacles and the in vivo or cadaver test will be performed with medical teams.

Additionally, the ability to vary the stiffness of continuum robots expands the design flexibility of surgical instruments. To adapt the instrument to carry specific interventional applications such as biopsy, brachytherapy, and therapy delivery, it is possible to utilize this mechanism to set the desired range of variable stiffness. For example, operators lower the stiffness during navigation and increase the stiffness during operating surgical devices or intervene process into the body. We plan to apply the mechanism to variable stiffness backbones and combine them with the stiffness control algorithms for continuum robots [34] to develop other surgical instruments in minimally invasive surgery.

REFERENCES

[1] J. Abadie, N. Chaillet, and C. Lexcellent, "Modeling of a new SMA micro-actuator for active endoscopy applications," *Mechatronics*, vol. 19, no. 4, pp. 437–442, 2009.

[2] Y. Chen, J. Sun, Y. Liu, and J. Leng, "Variable stiffness property study on shape memory polymer composite tube," *Smart Mater. Struct.*, vol. 21, no. 9, 2012, Art. no. 094021.

[3] Y. Shan et al., "Variable stiffness structures utilizing fluidic flexible matrix composites," *J. Intell. Mater. Syst. Struct.*, vol. 20, no. 4, pp. 443–456, 2009.

[4] O. Tabata et al., "Microfabricated tunable bending stiffness devices," *Sens. Actuators Phys.*, vol. 89, no. 1–2, pp. 119–123, 2001.

[5] H. Kim, H. Park, J. Kim, K.-J. Cho, and Y.-L. Park, "Design of anisotropic pneumatic artificial muscles and their applications to soft wearable devices for text neck symptoms," in *Proc. 39th Annu. Int. Conf. IEEE Eng. Medicine Biol. Soc.*, 2017, pp. 4135–4138.

[6] Y.-J. Park, T. M. Huh, D. Park, and K.-J. Cho, "Design of a variable-stiffness flapping mechanism for maximizing the thrust of a bio-inspired underwater robot," *Bioinspir. Biomim.*, vol. 9, no. 3, 2014, Art. no. 036002.

[7] A. Firouzeh and J. Paik, "Grasp mode and compliance control of an underactuated origami gripper using adjustable stiffness joints," *IEEEASME Trans. Mechatron.*, vol. 22, no. 5, pp. 2165–2173, Oct. 2017.

[8] Y. J. Kim, S. Cheng, S. Kim, and K. Iagnemma, "A stiffness-adjustable hyperredundant manipulator using a variable neutral-line mechanism for minimally invasive surgery," *IEEE Trans. Robot.*, vol. 30, no. 2, pp. 382–395, Apr. 2014.

[9] Y.-J. Kim, S. Cheng, S. Kim, and K. Iagnemma, "A novel layer jamming mechanism with tunable stiffness capability for minimally invasive surgery," *IEEE Trans. Robot.*, vol. 29, no. 4, pp. 1031–1042, Aug. 2013.

[10] N. G. Cheng et al., "Design and analysis of a robust, low-cost, highly articulated manipulator enabled by jamming of granular media," in *Proc. IEEE Int. Conf. Robot. Automat.*, 2012, pp. 4328–4333.

[11] A. J. Loeve, O. S. van de Ven, J. G. Vogel, P. Breedveld, and J. Dankelman, "Vacuum packed particles as flexible endoscope guides with controllable rigidity," *Granular Matter*, vol. 12, no. 6, pp. 543–554, 2010.

[12] S. Hauser, M. Robertson, A. Ijspeert, and J. Paik, "JammJoint: A variable stiffness device based on granular jamming for wearable joint support," *IEEE Robot. Automat. Lett.*, vol. 2, no. 2, pp. 849–855, Apr. 2017.

[13] T. Ranzani, M. Cianchetti, G. Gerboni, I. D. Falco, and A. Menciassi, "A soft modular manipulator for minimally invasive surgery: Design and characterization of a single module," *IEEE Trans. Robot.*, vol. 32, no. 1, pp. 187–200, Feb. 2016.

[14] R. Zhao, Y. Yao, and Y. Luo, "Development of a variable stiffness over tube based on low-melting-point-alloy for endoscopic surgery," *J. Med. Devices*, vol. 10, no. 2, 2016, Art. no. 021002.

[15] B. E. Schubert and D. Floreano, "Variable stiffness material based on rigid low-melting-point-alloy microstructures embedded in soft poly (dimethyl-siloxane) (PDMS)," *RSC Adv.*, vol. 3, no. 46, pp. 24671–24679, 2013.

[16] R. Steven, J. Sung-Hwan, P. Yong-Lae, and M. Carmel, "Liquid metal-conductive thermoplastic elastomer integration for low-voltage stiffness tuning," *Adv. Mater. Technol.*, vol. 2, no. 12, Oct. 2017, Art. no. 1700179.

[17] H. Dong and G. M. Walker, "Adjustable stiffness tubes via thermal modulation of a low melting point polymer," *Smart Mater. Struct.*, vol. 21, no. 4, 2012, Art. no. 042001.

[18] A. Orita and M. R. Cutkosky, "Scalable electroactive polymer for variable stiffness suspensions," *IEEEASME Trans. Mechatron.*, vol. 21, no. 6, pp. 2836–2846, Dec. 2016.

[19] N. Herzig, P. Maiolino, F. Iida, and T. Nanayakkara, "A variable stiffness robotic probe for soft tissue palpation," *IEEE Robot. Automat. Lett.*, vol. 3, no. 2, pp. 1168–1175, Apr. 2018.

[20] J. Kim, C. Kim, S. Kang, and K.-J. Cho, "A novel variable stiffness mechanism for minimally invasive surgery using concentric anisotropic tube structure," in *Proc. Hamlyn Symp. Medical Robot.*, 2017, pp. 43–44.

[21] T. Duerig, D. Stoeckel, and D. Johnson, "SMA: Smart materials for medical applications," in *Proc. Eur. Workshop Smart Struct. Eng. Technol.*, 2003, vol. 4763, pp. 7–16.

[22] J.-S. Kim, D.-Y. Lee, K. Kim, S. Kang, and K.-J. Cho, "Toward a solution to the snapping problem in a concentric-tube continuum robot: Grooved tubes with anisotropy," in *Proc. IEEE Int. Conf. Robot. Automat.*, 2014, pp. 5871–5876.

[23] D.-Y. Lee et al., "Anisotropic patterning to reduce instability of concentric-tube robots," *IEEE Trans. Robot.*, vol. 31, no. 6, pp. 1311–1323, Dec. 2015.

[24] P. Zhu, L. C. Brinson, E. Peraza-Hernandez, D. Hartl, and A. Stebner, "Comparison of three-dimensional shape memory alloy constitutive models: finite element analysis of actuation and superelastic responses of a shape memory alloy tube," in *Proc. ASME 2013 Conf. Smart Mater. Adaptive Struct. Intell. Syst.*, 2013, pp. V002T02A004–V002T02A004.

[25] H. Huang, H. Y. Zheng, and G. C. Lim, "Femtosecond laser machining characteristics of Nitinol," *Appl. Surf. Sci.*, vol. 228, no. 1–4, pp. 201–206, 2004.

[26] A. K. Dubey and V. Yadava, "Experimental study of Nd: YAG laser beam machining—An overview," *J. Mater. Process. Technol.*, vol. 195, no. 1–3, pp. 15–26, 2008.

[27] N. J. van de Berg, D. J. van Gerwen, J. Dankelman, and J. J. van den Dobbelsteen, "Design choices in needle steering—A review," *IEEEASME Trans. Mechatron.*, vol. 20, no. 5, pp. 2172–2183, Oct. 2015.

[28] R. J. Webster, J. Memisevic, and A. M. Okamura, "Design considerations for robotic needle steering," in *Proc. IEEE Int. Conf. Robot. Automat.*, 2005, pp. 3588–3594.

[29] P. Moreira, S. Patil, R. Alterovitz, and S. Misra, "Needle steering in biological tissue using ultrasound-based online curvature estimation," in *Proc. IEEE Int. Conf. Robot. Automat.*, 2014, vol. 2014, pp. 4368–4373.

This article has been accepted for inclusion in a future issue of this journal. Content is final as presented, with the exception of pagination.

KIM *et al.*: CONTINUOUSLY VARIABLE STIFFNESS MECHANISM USING NONUNIFORM PATTERNS ON COAXIAL TUBES   13

[30] I. Robert, J. Webster, J. S. Kim, N. J. Cowan, G. S. Chirikjian, and A. M. Okamura, "Nonholonomic modeling of needle steering," *Int. J. Robot. Res.*, vol. 25, no. 5–6, pp. 509–525, May 2006.
[31] A. Majewicz, J. J. Siegel, A. A. Stanley, and A. M. Okamura, "Design and evaluation of duty-cycling steering algorithms for robotically-driven steerable needles," in *Proc. IEEE Int. Conf. Robot. Automat.*, 2014, pp. 5883–5888.
[32] M. C. Bernardes, B. V. Adorno, P. Poignet, N. Zemiti, and G. A. Borges, "Adaptive path planning for steerable needles using duty-cycling," in *Proc. IEEE/RSJ Int. Conf. Intell. Robot. Syst.*, 2011, pp. 2545–2550.
[33] P. J. Swaney, J. Burgner, H. B. Gilbert, and R. J. Webster, "A flexure-based steerable needle: High curvature with reduced tissue damage," *IEEE Trans. Biomed. Eng.*, vol. 60, no. 4, pp. 906–909, Apr. 2013.
[34] M. Mahvash and P. E. Dupont, "Stiffness control of surgical continuum manipulators," *IEEE Trans. Robot.*, vol. 27, no. 2, pp. 334–345, Apr. 2011.

Sungchul Kang (M'06) received the B.S., M.S., and Ph.D. degrees in mechanical design and production engineering from Seoul National University, South Korea, in 1989, 1991, and 1998, respectively.

He has conducted robotics research in Korea Institute of Science and Technology from 1991 to 2019 and in Robot Center at Samsung Research since 2019. His research interests include manipulation for medical and service robots based on mechanism design and control.

Jongwoo Kim (S'14) received the B.S. and M.S.–Ph.D. degrees in mechanical and aerospace engineering from Seoul National University, Seoul, South Korea, in 2013 and 2019, respectively.

At present, he is a Postdoctoral Research Fellow with the Center for Image-Guided Innovation & Therapeutic Intervention, Hospital for Sick Children, Toronto, ON, Canada. His current research interests include surgical robotics, medical devices, soft robotics, and novel mechanisms using smart structures.

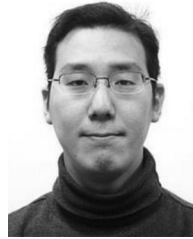Dr. Kim has received the Global Ph.D. Fellowship from the National Research Foundation of Korea.

Chunwoo Kim (M'18) received the B.S. degree in mechanical and aerospace engineering from Seoul National University, Seoul, South Korea, in 2008, and the Ph.D. degree in mechanical engineering from Johns Hopkins University, Baltimore, MD, USA, in 2014.

He is currently with the Center for Medical Robotics, Korea Institute of Science and Technology, Seoul, South Korea.

His research interests include image-guided robots, surgical robots, and medical devices.

Dr. Kim has received the Fulbright Scholarship and the Prostate Cancer Research Training Award of the United States Department of Defense.

Woo-Young Choi (S'15) received the B.S. and M.S. degrees in mechanical and aerospace engineering from Seoul National University, Seoul, South Korea, in 2015 and 2018, respectively.

His research interests include robotic systems using smart materials/actuators and novel mechanisms for soft robots.

Kyu-Jin Cho (M'08) received the B.S and M.S. degrees from Seoul National University, Seoul, South Korea, in 1998 and 2000, respectively, and the Ph.D. degree in mechanical engineering from the Massachusetts Institute of Technology, Cambridge, MA, USA, in 2007.

He was a Postdoctoral Fellow with the Harvard Microrobotics Laboratory until 2008. At present, he is a Professor of Mechanical and Aerospace Engineering and the Director of BioRobotics Laboratory and Soft Robotics Research Center with the Seoul National University. His research interests include biologically inspired robotics, soft robotics, soft wearable devices, novel mechanisms using smart structures, and rehabilitation and assistive robotics.

Dr. Cho has received the 2014 IEEE RAS Early Academic Career Award, 2014 ASME Compliant Mechanism Award, 2013 IROS Best Video Award, and 2013 KSPE Paik Am Award.